

CO Excitation and Line Energy Distributions in Gas-selected Galaxies

A. Klitsch,^{1*} L. Christensen,^{2,3} F. Valentino,^{2,3} N. Kanekar,⁴ P. Møller,^{3,5} M. A. Zwaan,⁵ J. P. U. Fynbo,^{2,3} M. Neeleman,⁶ J. X. Prochaska^{7,8}

¹*DARK, Niels Bohr Institute, University of Copenhagen, Jagtvej 128, 2200 Copenhagen N, Denmark*

²*Cosmic Dawn Center (DAWN), Denmark,*

³*Niels Bohr Institute, University of Copenhagen, Jagtvej 128, 2200 Copenhagen N, Denmark*

⁴*National Centre for Radio Astrophysics, TIFR, Post Bag 3, Ganeshkhind, Pune 411 007, India*

⁵*European Southern Observatory, Karl-Schwarzschildstrasse 2, D-85748 Garching bei München, Germany*

⁶*Max-Planck-Institut für Astronomie, Königstuhl 17, D-69117, Heidelberg, Germany*

⁷*Department of Astronomy & Astrophysics, UCO/Lick Observatory, University of California, 1156 High Street, Santa Cruz, CA 95064, USA*

⁸*Kavli Institute for the Physics and Mathematics of the Universe (Kavli IPMU), The University of Tokyo, 5-1-5 Kashiwanoha, Kashiwa, 277-8583, Japan*

Accepted XXX. Received YYY; in original form ZZZ

ABSTRACT

While emission-selected galaxy surveys are biased towards the most luminous part of the galaxy population, absorption selection is a potentially unbiased galaxy selection technique with respect to luminosity. However, the physical properties of absorption-selected galaxies are not well characterised. Here we study the excitation conditions in the interstellar medium (ISM) in damped Ly α (DLA) absorption-selected galaxies. We present a study of the CO spectral line energy distribution (SLED) in four high-metallicity absorption-selected galaxies with previously reported CO detections at intermediate ($z \sim 0.7$) and high ($z \sim 2$) redshifts. We find further evidence for a wide variety of ISM conditions in these galaxies. Two out of the four galaxies show CO SLEDs consistent with that of the Milky Way inner disk. Interestingly, one of these galaxies is at $z \sim 2$ and has a CO SLED below that of main-sequence galaxies at similar redshifts. The other two galaxies at $z > 2$ show more excited ISM conditions, with one of them showing thermal excitation of the mid- J ($J = 3, 4$) levels, similar to that seen in two massive main-sequence galaxies at these redshifts. Overall, we find that absorption selection traces a diverse population of galaxies.

Key words: galaxies: evolution - galaxies: formation - galaxies: high redshift - galaxies: ISM

1 INTRODUCTION

Conventional galaxy surveys identify galaxies based on the stellar or dust continuum emission and are therefore biased towards the luminous part of the galaxy population. Depending on the survey characteristics the emission selection tends to pick out high stellar mass galaxies with high star-formation rates (SFRs). An alternative and potentially unbiased galaxy selection technique with respect to stellar mass is from the absorption signature that the gas content of a galaxy and its circumgalactic medium imprints in the spectra of otherwise unrelated background quasars (damped Ly α absorbers with an atomic hydrogen column density of $N(\text{H I}) \geq 2 \times 10^{20} \text{ cm}^{-2}$; Wolfe et al. 2005). A good understanding of the underlying galaxy population traced by absorption selection is required to draw firm conclusions on galaxy evolution.

Absorption-selected galaxies at intermediate redshifts ($z \sim 0.5$) were found to be extremely molecular gas-rich with low star formation efficiencies compared to emission-selected galaxies at low- ($z \sim 0$) and high ($z \sim 2$) redshifts (Møller et al. 2018; Kanekar et al. 2018; Péroux et al. 2019; Szakacs et al. 2021). In these studies each

individual (sub-)DLA system was detected in a single CO rotational transition [CO(1–0), (2–1), (3–2) or (4–3)]. Most authors have used CO line ratios and CO-to-H₂ conversion factors (α_{CO}) appropriate for the Milky Way to derive molecular gas masses (Kanekar et al. 2018; Møller et al. 2018; Fynbo et al. 2018; Péroux et al. 2019). Szakacs et al. (2021) have used a CO line ratio appropriate for the Milky Way but derived an α_{CO} conversion factor based on the gas metallicity.

At higher redshifts, $z \approx 2 - 4$, there have recently been a few detections of CO emission in absorption-selected galaxies associated with high-metallicity absorbers (Neeleman et al. 2018, 2020; Fynbo et al. 2018; Kanekar et al. 2020). Again, each individual DLA system was detected in a single CO rotational transition [CO(2–1), (3–2) or (4–3)]. Here the authors have used a CO line ratio appropriate for galaxies near the main sequence at $z = 0 - 3$ and $\alpha_{\text{CO}} = 4.36 \text{ M}_{\odot} (\text{K km s}^{-1} \text{ pc}^2)^{-1}$, applicable for galaxies with a near solar metallicity that are not undergoing a star burst (Tacconi et al. 2020; Bolatto et al. 2013).

Klitsch et al. (2019) studied the CO spectral line energy distribution (CO SLED) of three absorption-selected galaxies at $z \sim 0.5$. In two out of three galaxies they found higher excitation than in the interstellar medium (ISM) of the Milky Way. These galaxies have

* E-mail: anne.klitsch@gmail.com

indeed been suggested to host an active nucleus and/or a starburst (Burbidge et al. 1996; Chen et al. 2005), consistent with the high CO excitation. This suggests that using line ratios from the Milky Way and α_{CO} applicable for normal star-forming galaxies might not be appropriate for all absorption-selected galaxies. It is clear that the gas mass measurements critically depend on the assumptions for excitation conditions and CO-to-H₂ conversion factor. CO SLED studies are key to determine the CO excitation and thus obtain accurate estimates of the molecular gas mass.

CO SLED studies conducted so far include the Milky Way and nearby galaxies (e.g. Fixsen et al. 1999; Bayet et al. 2004; van der Werf et al. 2010; Greve et al. 2014; Kamenetzky et al. 2014, 2017; Rosenberg et al. 2015; Lu et al. 2017), normal star-forming galaxies at higher redshifts $z > 1.5$ (Daddi et al. 2015; Brisbin et al. 2019; Henríquez-Brocal et al. 2021), lensed main-sequence galaxies (Dessauges-Zavadsky et al. 2015) and more extreme objects such as submillimetre galaxies, starburst galaxies and quasars (e.g. Weiß et al. 2005; Ivison et al. 2011; Bothwell et al. 2013; Harrington et al. 2021). It has been found that the CO excitation in high redshift galaxies is typically higher than in the inner disk of the Milky Way. Recently, Valentino et al. (2020) reported CO emission line ratios for galaxies on and above the main sequence for star-forming galaxies at $z \sim 1.5$. They obtained CO excitation ratios above that typically observed in the inner disk of the Milky Way. They find that the CO excitation is mainly driven by enhanced SFRs and compact galaxy sizes resulting in enhanced dense molecular gas fractions and higher dust and gas temperatures. Similarly, Boogaard et al. (2020) conducted a study of CO SLEDs in galaxies detected in the untar-geted ALMA Spectroscopic Survey in the Hubble Ultra Deep Field (ASPECS; Aravena et al. 2019). The galaxies in their sample lie on, above or below the main-sequence (Boogaard et al. 2020; Aravena et al. 2019; Aravena et al. 2020). Boogaard et al. (2020) report an average CO SLED at $z = 1.2$ lower than that of the *BzK*-colour-selected galaxies at $z = 1.5$ (Daddi et al. 2015) but above that of the Milky Way inner disk. At higher redshift ($z = 2.5$) Boogaard et al. (2020) find a steeper CO SLED similar to that of local starburst galaxies and the low end of the excitation range observed in sub-mm galaxies (SMGs) at a similar redshift. According to the authors this result seems not to be due to the CO flux-selection. The above results suggest an intrinsic evolution of the ISM excitation conditions, with typical high-redshift galaxies having higher CO excitation than that seen in the inner disk of the Milky Way.

Absorption selection preferentially identifies lower-mass galaxies that lie on or below the main sequence of star-forming galaxies at their respective redshifts (e.g. Krogager et al. 2017; Kanekar et al. 2018; Rhodin et al. 2018, 2021). However, the detections of CO emission in absorption-selected galaxies (especially at $z \gtrsim 2$) were obtained in the highest-metallicity absorbers, and thus may contain a bias towards object with higher stellar masses (Kanekar et al. 2020). It is therefore not clear if CO SLEDs inferred from emission-selected galaxy samples are appropriate for absorption-selected galaxies, too.

The goal of this study is to characterise the CO SLEDs of absorption-selected galaxies that have been detected in CO emission in previous studies, using higher-order CO rotational transitions that are observable with the Atacama Large Millimeter/submillimeter Array (ALMA). The targets are selected irrespective of their redshift and the full sample includes six galaxies, three at intermediate redshift ($z \sim 0.5$) and three at high redshift ($z \sim 2$). In this work, we report observations of four galaxies, one at $z \sim 0.7$ and three at $z \sim 2 - 2.5$.

The structure of this paper is as follows: We present the observations and data reduction in Section 2 and the source detections,

Table 1. Details of the new ALMA observations.

DLA galaxy	CO line	ν [GHz]	RMS [mJy beam ⁻¹]	Beam ^a [″ × ″]	Beam ^b [kpc × kpc]
J2335+1501	3–2	205.86	0.56	1.8×1.5	13×11
B0551–366	5–4	194.58	0.58	1.8×1.4	15×12
B0551–366	6–5	233.44	0.44	1.4×1.2	12×10
B0551–366	7–6	272.32	0.36	1.4×1.1	11×9
B1228–113	6–5	216.54	0.27	1.6×1.2	13×10
J0918+1636	4–3	128.68	0.47	1.4×1.1	11×9
J0918+1636	5–4	160.84	0.54	1.1×0.76	9×6

Notes: ν is the central observing frequency of the spectral window covering the redshifted CO line, in GHz, RMS is the RMS noise in the centre of the field quoted in mJy beam⁻¹ per 40 km s⁻¹ channel, ^aThe FWHM of the clean beam, equivalent to the angular resolution in arcsec. ^bThe spatial resolution at the absorber redshift.

CO emission line measurements, and CO line ratios in Section 3. In Section 4, we discuss the implications of our results for studies of absorption-selected galaxies.

Throughout the paper, we adopt a flat Λ -Cold Dark Matter cosmological model with $H_0 = 70$ km s⁻¹ Mpc⁻¹, $\Omega_m = 0.3$, and $\Omega_\Lambda = 0.7$ and a Chabrier (2003) initial mass function (IMF).

2 OBSERVATIONS AND DATA REDUCTION

We observe one or more higher J rotational transitions from a sample of absorption-selected galaxies previously detected in CO emission (Neeleman et al. 2018; Fynbo et al. 2018; Kanekar et al. 2018; Kanekar et al. 2020) to study the excitation conditions in the ISM using the CO SLEDs. The original targets were selected from damped or sub-damped Ly α absorption systems having relatively high metallicities, above 10 per cent solar. This is because high-metallicity absorbers are expected to be associated with more massive galaxies (Møller et al. 2013; Christensen et al. 2014), which are consequently expected to have both larger molecular gas masses and lower α_{CO} values. CO emission was typically detected in the fields of absorbers with the highest metallicities, $[M/H] \gtrsim -0.25$. The detection fraction of CO emission in these absorption-selected galaxies is 5/7 in the intermediate-redshift sample (Kanekar et al. 2018) and 5/12 in the high-redshift sample (Kanekar et al. 2020). Targets with non-detections of CO emission have molecular gas masses $< 5 \times 10^9 M_\odot$ and $< 10^{10} M_\odot$ in the intermediate- z and high- z samples, respectively (Kanekar et al. 2018; Kanekar et al. 2020).

The ALMA observations are carried out under program 2019.1.01457.S (PI: L. Christensen) and the observed fields and transitions are listed in Table 1. Two fields are observed in one new CO transition, one field in two CO transitions, and one in three CO transitions. All observations use four 1.875 GHz wide spectral windows, with one spectral window (in FDM mode of the correlator) covering the expected redshifted CO line frequency, and the other three spectral windows (in TDM mode) placed at neighbouring frequencies to measure the continuum emission.

We use the pipeline calibrated *uv*-data sets, as delivered by the Joint ALMA Observatory. Additional data reduction steps are carried out with the Common Astronomy Software Applications (CASA) software package version 5.6 (McMullin et al. 2007). In the case of PKS B1228–113, the QSO continuum flux density is sufficient to self-calibrate the visibilities, and thus improve our estimates of

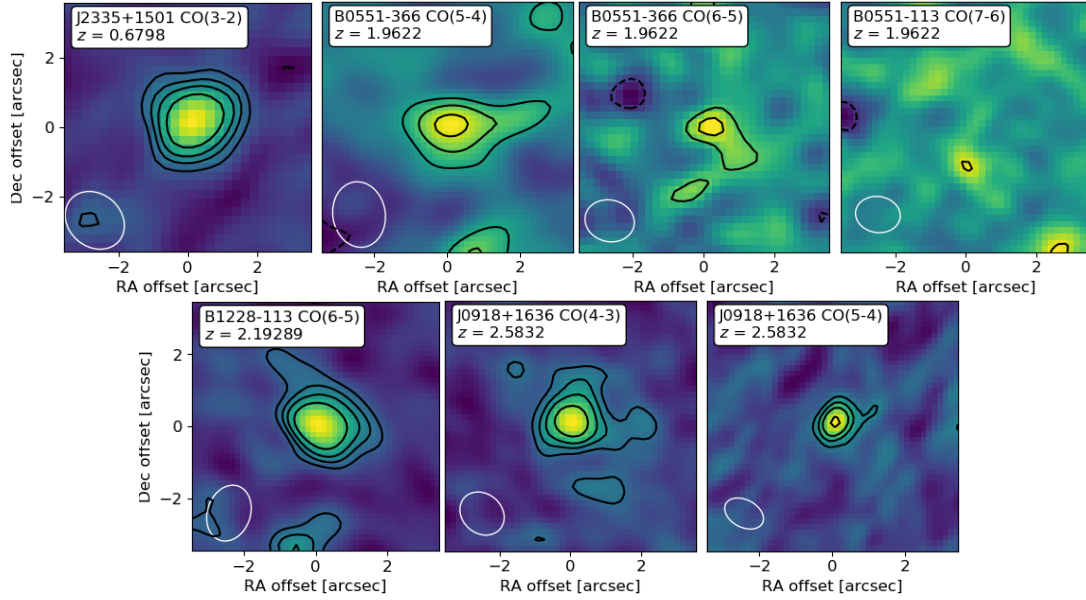


Figure 1. Integrated CO line flux density maps of the four detected galaxies. The maps are calculated by integrating over the velocity channels marked in yellow in Fig. 2. For the non-detected CO(7–6) transition in DLA B0551-113 we integrate over the same velocity range as for the CO(6–5) transition. Black contours mark the 3, 5, 7 and 10 σ levels. Negative contours are shown as dashed lines. The white ellipse shows the synthesized beam.

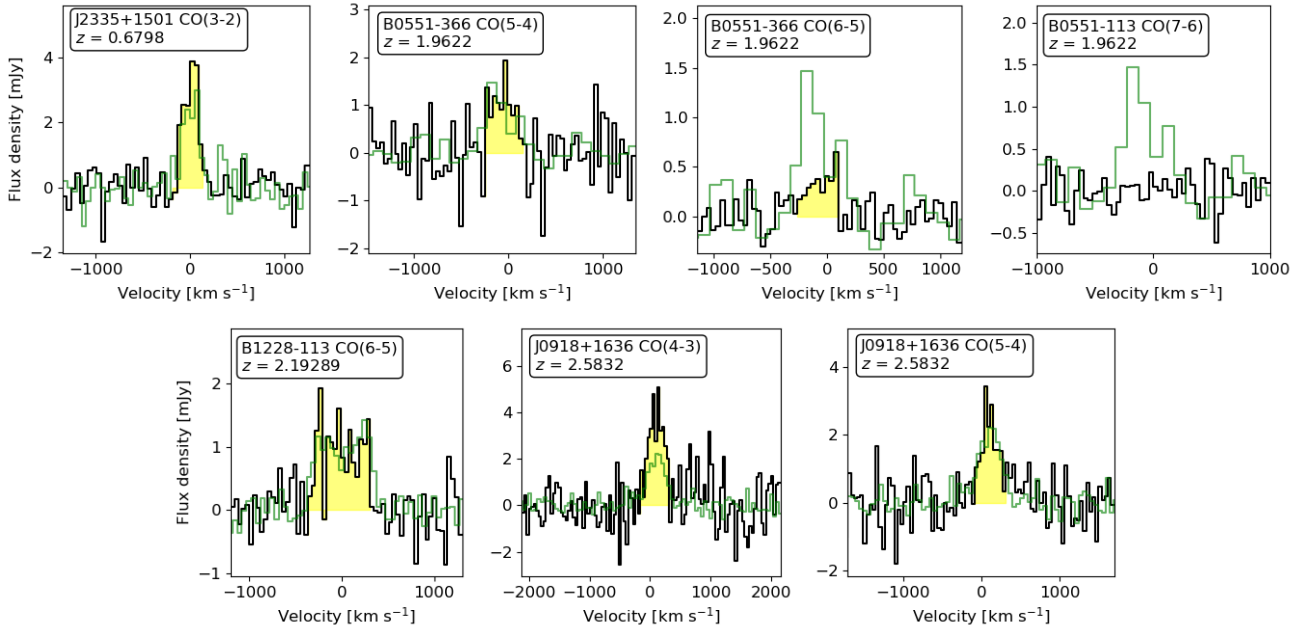


Figure 2. CO emission line spectra of the four detected galaxies. As a comparison we show the new CO line observations from this work (black) and the previously observed CO lines (green; Kanekar et al. 2018; Kanekar et al. 2020). The yellow area marks the channels used for calculating the integrated flux density. It can be seen that the line centres and widths measured from the different CO transitions agree well. For CO(7–6) from B0551-113 we show the spectrum extracted within one beam at the position of the absorber host galaxy.

the antenna-based gains over those obtained from the pipeline calibration. The self-calibration is done using the routine `GAINCALR` (Chowdhury et al. 2020), following a standard iterative imaging and self-calibration procedure. For all fields, continuum images are made from the line-free spectral windows with the `TCLEAN` routine, using “Briggs” weighting (Briggs 1995) with a “robust” parameter of 0.5. The continuum is subtracted from the calibrated spectral-line visibilities using the routine `UVSUB`. The continuum-subtracted visibilities

are then imaged, at a velocity resolution of 40 km s^{-1} , cleaning down to 0.5σ , where σ is the RMS noise per 40 km s^{-1} channel. Natural weighting is used, to obtain the maximum sensitivity, appropriate for a line detection experiment for unresolved sources. Any residual continuum emission is subtracted from the spectral cubes by fitting a first-order polynomial to line-free channels, using the routine `IMCONTSUB`. The final beam sizes as well as the RMS noise per 40 km s^{-1} channel at the centre of each field are listed in Table 1. The systematic

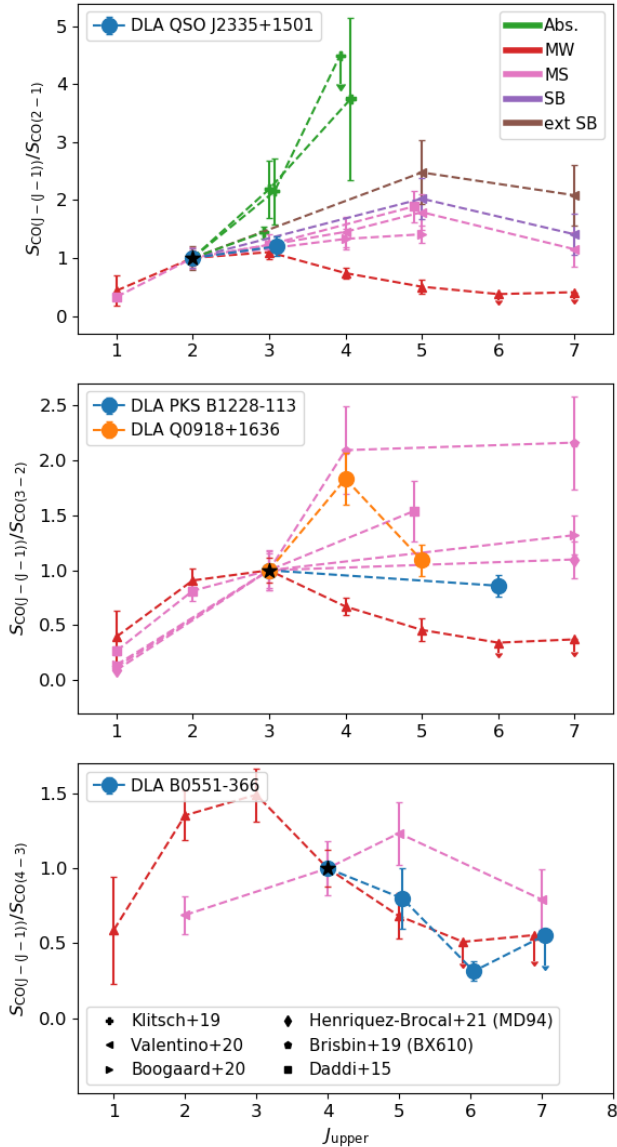


Figure 3. CO SLEDs of absorption-selected galaxies. We note that due to the missing CO(1–0) flux density measurement these plots are normalized to the lowest available CO transition (black star). The CO SLEDs of the inner disk of the Milky Way (red; [Fixsen et al. 1999](#)), other absorption-selected galaxies at $z \sim 0.5$ (green; [Klitsch et al. 2019](#)), main-sequence galaxies at $z = 1.2 - 2.2$ (pink; [Daddi et al. 2015](#); [Brisbin et al. 2019](#); [Boogaard et al. 2020](#); [Valentino et al. 2020](#); [Henríquez-Brocal et al. 2021](#)), starburst (purple) and extreme starburst (brown) galaxies at $z \sim 1.5$ ([Valentino et al. 2020](#)) are shown for comparison (colours differentiate object classes, while symbols indicate literature references). Arrows show the three sigma upper limits. We find that absorption-selected galaxies cover a broad range of excitation conditions.

uncertainty on the flux density scale in the ALMA bands used here is assumed to be 5 per cent (ALMA Technical Handbook¹), which we interpret as a 2σ error.

¹ <https://almascience.nrao.edu/documents-and-tools/cycle7/alma-technical-handbook>

3 ANALYSIS

We perform an automatic source finding on the spectral windows covering the targeted CO line using the SoFIA source finding application ([Serra et al. 2015](#)) developed for H I interferometric observations. We use the standard configuration of the ‘Smooth + Clip Finder’ with a 4σ detection threshold. We detect all known absorption-selected galaxies in each field in all observed CO transitions except for the CO(7–6) transition in DLA B0551-366. Apart from these previously reported galaxies, we do not find any additional galaxies.

In particular, we search for CO emission from the low-impact parameter ($b \approx 16$ kpc) absorption-selected galaxy in the J0918+1636 field ([Fynbo et al. 2013](#)). This galaxy was not detected in CO(3–2) emission by [Fynbo et al. \(2018\)](#). However, we do not detect CO(4–3) emission from this galaxy. [Fynbo et al. \(2018\)](#) report another galaxy at the same redshift as the absorber, located at a larger impact parameter of 117 kpc which we here refer to as DLA J0918+1636.

We measure the CO line flux densities of the previously reported galaxies with CO detections in order to examine their CO SLEDs. Integrated CO line flux density maps and CO spectra of the galaxies are shown in Figs. 1 and 2, respectively. We determined the optimal velocity range for the flux density maps covering the entire CO emission line in an iterative manner. The spectra are extracted from a region defined by the 3σ contour in the integrated flux density images. Details of the detections are listed in Table 2. The line full-widths-at-half-maximum (FWHMs) are determined directly from the extracted spectra shown in Fig. 2, by measuring the width of the line profile at 50 per cent of the peak flux density.

We compare the spectral line shape of the different CO transitions reported in this work with those of the lower- J lines in the literature (see Fig. 2). The line centres and FWHMs of the various transitions reported in Table 3 agree within the uncertainties with the measurements from the lower- J lines.

3.1 CO Excitation and Line Energy Distribution

Using the previously reported mid- J rotational transitions we calculate the CO line flux density and luminosity ratios of the different available transitions for each absorber. The CO(1–0) transition that is traditionally used for this comparison is not available for any of our targets. We therefore calculate the line luminosity ratios $L'_{\text{CO}(u-[u-1])}/L'_{\text{CO}(l-[l-1])} = r_{ul}$, where u is the upper J level of the higher available rotational transition and l is the upper J level of the lower available transition. The line ratios are reported in Table 3, where the reported uncertainties on the line ratios include the flux density errors in each transition. The same ratios for the inner disk of the Milky Way based on CO line observations ([Fixsen et al. 1999](#)) are also listed in Table 3. For high J CO transitions [CO(6–5) and CO(7–6)] in the Milky Way inner disk we list the 3σ upper limits ([Fixsen et al. 1999](#)).

The line ratios in two out of our four absorption-selected galaxies (DLA J2335+1501 and DLA B0551-366) are consistent with the same line ratios for the Milky Way inner disk. The line luminosity ratios in the absorption-selected galaxies DLA B1228-113 and DLA J0918+1636 are significantly above that of the Milky Way inner disk. However, we note that line ratios involving neighbouring J transitions can be ambiguous especially in the mid- and high- J transitions where the gradient in the excitation ladder is smoother than at low J .

In addition to the Milky Way CO line luminosity ratios, we compare the line flux density ratios in Table 3 with the CO SLEDs of dif-

Table 2. Overview of physical properties of the absorption-selected galaxies.

DLA galaxy	z_{QSO}	z_{abs}	RA	Dec	CO line	b [kpc]	FWHM [km s ⁻¹]	S_{int} [Jy km s ⁻¹]	S_{peak} [mJy]	$L'_{\text{CO}} \times 10^9$ [K km s ⁻¹ pc ²]
J2335+1501	0.791	0.6798	23h35m44.19s	+15d01m14.3s	3–2	29	226 ± 45	0.722 ± 0.066	3.88 ± 0.50	1.97 ± 0.18
B0551–366	2.317	1.9622	05h52m46.17s	–36d37m25.9s	5–4	14	357 ± 40	0.346 ± 0.078	1.93 ± 0.60	2.64 ± 0.60
					6–5		239 ± 40	0.136 ± 0.023	0.76 ± 0.21	0.72 ± 0.12
					7–6		n.a.	< 0.24	n.a.	< 0.93
B1228–113	3.528	2.1929	12h30m57.07s	–11d39m29.0s	6–5	28	595 ± 40	0.624 ± 0.064	1.92 ± 0.37	4.01 ± 0.41
J0918+1636	3.096	2.5832	09h18m26.26s	+16d35m55.4s	4–3	117	320 ± 40	1.35 ± 0.15	5.1 ± 1.0	25.9 ± 2.9
					5–4		119 ± 40	0.803 ± 0.092	3.43 ± 0.69	9.9 ± 1.1

Notes: b denotes the impact parameter between the quasar sightline and the position of the galaxy, FWHM is the width of the CO emission line at 50 percent of the peak flux density, sometimes also referred to as W_{50} , S_{int} is the integrated line flux density, S_{peak} is the peak flux density of the line, L'_{CO} denotes the line luminosity of the observed transition, errors on the last three quantities include a 2.5 per cent error on the absolute flux density scale. We quote a 3σ upper limit for the CO(7–6) emission line flux density in DLA B0551–366 adopting the same FWHM as in the CO(6–5) emission line.

Table 3. Comparison to previous observations and CO line luminosity ratios.

DLA galaxy	CO line	FWHM [km s ⁻¹]	S_{int} [Jy km s ⁻¹]	S_u/S_l	$L'_{\text{CO}} \times 10^9$ [K km s ⁻¹ pc ²]	r_{ul}	$r_{\text{ul}}^{\text{MW}}$	Ref.
J2335+1501	2–1	250 ± 50	0.601 ± 0.064	1	3.70 ± 0.40	1	1	Kanekar et al. (2018)
	3–2	226 ± 45	0.722 ± 0.066	1.20 ± 0.17	1.97 ± 0.18	0.532 ± 0.075	0.490 ± 0.058	This work
B0551–366	4–3	300 ± 25	0.433 ± 0.052	1	5.15 ± 0.62	1	1	Kanekar et al. (2020)
	5–4	357 ± 40	0.346 ± 0.078	0.80 ± 0.20	2.64 ± 0.60	0.51 ± 0.13	0.437 ± 0.098	This work
	6–5	239 ± 40	0.136 ± 0.023	0.314 ± 0.065	0.72 ± 0.12	0.140 ± 0.029	< 0.23	This work
	7–6	n.a.	< 0.24	< 0.55	< 0.93	< 0.17	< 0.18	This work
B1228–113	3–2	600 ± 22	0.726 ± 0.031	1	18.69 ± 0.80	1	1	Neeleman et al. (2018)
	6–5	595 ± 40	0.624 ± 0.064	0.860 ± 0.095	4.01 ± 0.41	0.215 ± 0.024	< 0.086	This work
J0918+1636	3–2	350 ± 25	0.736 ± 0.045	1	25.1 ± 1.6	1	1	Fynbo et al. (2018)
	4–3	320 ± 40	1.35 ± 0.15	1.83 ± 0.24	25.9 ± 2.9	1.03 ± 0.13	0.377 ± 0.045	This work
	5–4	119 ± 40	0.803 ± 0.092	1.09 ± 0.14	9.9 ± 1.1	0.394 ± 0.051	0.165 ± 0.037	This work

Notes: FWHM denotes the width of the line at 50 per cent of the peak line flux density. S_{int} is the integrated line flux density. S_u/S_l is the line flux density ratio that is also plotted in Fig. 3. L'_{CO} is the line luminosity of the given CO transition; values from Kanekar et al. (2018) and Kanekar et al. (2020) are scaled to the cosmology used in this paper. r_{ul} is the line luminosity ratio between the CO transition in the respective row and the lowest observed CO transition for that galaxy; $r_{\text{ul}}^{\text{MW}}$ denotes the same line luminosity ratio measured in the inner disk of the Milky Way (Fixsen et al. 1999). Limits on the line luminosity ratio are 3σ upper limits.

ferent galaxy types in Fig 3. The CO SLEDs of absorption-selected galaxies from this work are compared to the CO SLEDs of three absorption-selected galaxies at $z \sim 0.5$ (Klitsch et al. 2018, 2019), the inner disk of the Milky Way (Fixsen et al. 1999), main-sequence galaxies at $z = 1.2 - 2.2$ (Daddi et al. 2015; Brisbin et al. 2019; Boogaard et al. 2020; Valentino et al. 2020; Henríquez-Brocal et al. 2021), starburst and extreme starburst galaxies at $z \sim 1.5$ (Valentino et al. 2020). Again, we anchor the CO SLED to the lowest available transition for the different absorption-selected galaxies.

It can be seen that two out of the four CO SLEDs of absorption-selected galaxies have low excitation conditions consistent with that of the Milky Way inner disk and the other two show higher excitation. In the following we analyse the CO SLEDs of the different galaxies in more detail.

The lowest redshift galaxy in our sample, DLA J2335+150 at $z = 0.6798$, has a ratio that is consistent within the errors with the CO SLED of the Milky Way inner disk, but is also consistent with more excited CO SLEDs reported for galaxies on and above the star-forming main sequence at $z \sim 1.2 - 1.5$ (Daddi et al. 2015;

Boogaard et al. 2020; Valentino et al. 2020). Measurements of higher J transitions are required for this galaxy to test whether the CO SLED is similar to that of the Milky Way inner disk. The CO SLED of DLA B0551–366 at $z = 1.9622$ is consistent with the 3σ upper limits of the Milky Way inner disk but below the average CO SLED of main sequence galaxies at $z \sim 1.5$ (Valentino et al. 2020). The CO SLED of DLA B1228–113 at $z = 2.1929$ is below the CO SLED of main sequence galaxies at $z \sim 1.5$ and $z \sim 2.5$ but above that of the Milky Way inner disk. Finally, the CO SLED of DLA J0918+1636 at $z = 2.5832$ has an approximately thermal r_{43} while r_{53} is less than unity, but significantly above r_{53}^{MW} . This suggests that the CO SLED of DLA J0918+1636 is likely to be thermalised up to the $J = 4$ rotational level. We note that these are neighbouring mid- J CO transitions and that the main-sequence galaxy BX610 shows a similar r_{43} luminosity ratio, also consistent with thermal excitation (Brisbin et al. 2019). Further, observations of the lower- J lines are not available for DLA B0551–366 and of the intermediate- J lines for DLA B1228–113. We are therefore unable to determine the slope and the peak of the CO SLEDs in these galaxies. A better sampling

of the CO SLED in these galaxies, as well as observations of the CO $J(1-0)$ line in all our targets, are crucial to better understand the CO line excitation.

CO SLEDs are non-linear, non-monotonic functions with changing slopes as a function of the upper-state rotational quantum number J and different maxima for different object classes. Therefore we caution that differences in the CO SLEDs as well as line luminosity ratios r_{ul} anchored on higher J rotational transitions (above the CO(1–0) transition) can appear less pronounced. As an example r_{74} of the main-sequence galaxies at $z \sim 1.2$ (Valentino et al. 2020) is consistent with that of the Milky Way inner disk while the r_{72} ratio is above that of the Milky Way inner disk. Additionally, the incomplete sampling of CO SLEDs in different types of galaxies does not allow a direct comparison between all object classes. Even the class of main-sequence galaxies presented in Fig. 3 (middle panel) shows a wide range of excitation conditions.

3.2 SED Fitting

In addition to the CO line emission, we detected continuum emission from the absorber host galaxies DLA B1228–113 and DLA J0918+1636. The continuum images are shown in Fig. A1 and the flux density measurements are listed in Table A1.

We used MAGPHYS, (optimised for high-redshift galaxies; da Cunha et al. 2008, 2015) to carry out a fit to the broad-band spectral energy distributions (SEDs) of DLA J0918+1636 and DLA B1228–113, assuming a Chabrier (2003) IMF. All input values for the SED fits are listed in Table A1, the SED fit is shown in Fig. A2 and the best fitting results are listed in Table A2.

For DLA J0918+1636 at $z = 2.5832$ galaxy, we combine the new ALMA 2mm flux density with the existing optical and near-IR photometry (Fynbo et al. 2018). We obtain a stellar mass of $\log(M_\star/M_\odot) = 10.49^{+0.16}_{-0.11}$, consistent with the estimate in Fynbo et al. (2018). Our fit yields an SFR of $229^{+151}_{-91} M_\odot \text{ yr}^{-1}$, higher than the earlier estimate, albeit consistent within the errors.

For DLA B1228–113 at $z = 2.1929$, we combine our ALMA 1.3 mm flux density measurement with the 3 mm measurement of Neeleman et al. (2018), and use Very Large Telescope Multi Unit Spectroscopic Explorer (VLT/MUSE) archival data (programme ID 197.A-84, PI: Fumagalli) for the optical photometry. From the MUSE data cube, we extract a one-dimensional spectrum at the location of the galaxy within a $1''$ aperture diameter and integrate this with the Sloan Digital Sky Survey (SDSS) filter transmission curves to derive AB magnitudes $g = 25.3 \pm 0.3$, $r = 24.7 \pm 0.2$ and $i = 24.4 \pm 0.3$ for the galaxy. The photometry is corrected for a Galactic reddening $E_{B-V} = 0.0335$ (Schlafly & Finkbeiner 2011). The best SED fit with MAGPHYS yields a stellar mass of $\log(M_\star/M_\odot) = 10.13^{+0.34}_{-0.23}$ and a total SFR of $87^{+39}_{-28} M_\odot \text{ yr}^{-1}$, in agreement with the dust-corrected SFR derived from the H α emission (Neeleman et al. 2018).

MAGPHYS also returns dust masses of $\log(M_{\text{dust}}/M_\odot) = 8.74^{+0.10}_{-0.12}$ for DLA B1228–113, and $\log(M_{\text{dust}}/M_\odot) = 8.62^{+0.16}_{-0.15}$ for DLA J0918+1636. These are inferred from the optical-to-sub-mm photometry by assuming energy balance. However, we currently do not have any measurements probing the peak of the far IR emission and, thus, the dust temperature and total IR luminosity are not well-constrained.

To avoid possible overfitting of the far-IR regime, we derived an alternative estimate of M_{dust} by simply rescaling the observed photometry in the mm regime — probing the Rayleigh-Jeans tail of the dust emission — with a modified black body curve (MBB; Berta et al. 2016). We assumed $\beta = 1.8$

(e.g. Berta et al. 2016; Scoville et al. 2016) and a dust mass absorption coefficient of $k_0 = 5.1 \text{ cm}^2 \text{ g}^{-1}$ at rest-frame $\nu_0 = 250 \mu\text{m}$ consistent with Magdis et al. (2012). For $T_{\text{dust}} = 35 \text{ K}$ typical for galaxies at $z \sim 2-2.5$ (Schreiber et al. 2018 and references therein), we find $\log(M_{\text{dust}}/M_\odot) = 8.83 \pm 0.28$ for DLA B1228–113 and $\log(M_{\text{dust}}/M_\odot) = 8.72 \pm 0.27$ for DLA J0918+1636. The uncertainties mark the maximal fluctuation of M_{dust} obtained by allowing for $T_{\text{dust}} = 35 \pm 5 \text{ K}$ and $\beta = 1.8 \pm 0.2$. Variations in the dust mass absorption coefficient could induce an extra uncertainty of $\geq 0.18 \text{ dex}$ (Andersen 2007). Statistical uncertainties on the photometric measurements are $\approx 0.09 \text{ dex}$ and $\approx 0.14 \text{ dex}$ for DLA B1228–113 and DLA J0918+1636, respectively.

The MBB rescaling also allows us to estimate the luminosity at rest-frame $850\text{-}\mu\text{m}$, $L_{850\mu\text{m}}$, recently proposed as a dust (and gas) mass tracer (Scoville et al. 2016). Here we use $L_{850\mu\text{m}}$ to predict the expected $L'_{\text{CO}(1-0)}$ luminosity, assuming that our targets follow the same relation within a factor of two (Kaasinen et al. 2019). This yields $\log(L_{850\mu\text{m}}/\text{erg s}^{-1} \text{ Hz}^{-1}) = 30.80 \pm 0.12$ and 30.88 ± 0.13 for DLA B1228–113 and DLA J0918+1636, respectively, assuming the same ranges of T_{dust} and β as above.

3.3 Dust-Based CO Luminosities and Molecular Gas Masses

We derive the CO(1–0) luminosity, $L'_{\text{CO}(1-0)}$, based on the rest frame $850\mu\text{m}$ luminosity following the prescription of Scoville et al. (2016). This allows us to compare the $L'_{\text{CO}(1-0)}$ value inferred from the dust continuum emission (i.e. $L'_{850\mu\text{m}}$ with that ($L'_{\text{CO}(1-0)}^{\text{mid-}J \text{ CO}}$) derived from the measured luminosity of the mid- J CO transitions. The results are presented in Table 4. We note that Scoville et al. (2016) argue that a single scaling factor is applicable for galaxies with a stellar mass of $M_\star > 2 \times 10^{10} M_\odot$ irrespective of redshift and galaxy type.

For both galaxies, the CO luminosities derived from the two methods do not agree within the errors. While Kanekar et al. (2020) used sub-thermal CO line ratios to infer the CO(1–0) line luminosity, we show in Fig. 3 and Table 3 that DLA J0918+1636 shows thermalised CO excitation conditions for the $J = 4$ level relative to the $J = 3$ level. This suggests that, both mid- J levels would also show thermal excitation relative to the $J = 1$ level (i.e. that $r_{41} \approx 1$ and $r_{31} \approx 1$, rather than $r_{31} \approx 0.55$, as assumed by Kanekar et al. 2020). Adopting this line ratio results in a factor of ≈ 1.8 lower $L'_{\text{CO}(1-0)}$ than the estimate of Kanekar et al. (2020), i.e. $L'_{\text{CO}(1-0)} \approx (2.51 \pm 0.16) \times 10^{10} \text{ K km s}^{-1} \text{ pc}^2$. This is consistent with the estimate of the CO(1–0) line luminosity from the rest frame $850\text{-}\mu\text{m}$ luminosity. For DLA B1228–113 our observations only cover the CO(3–2) and CO(6–5) transitions. However, the agreement between the $L'_{850\mu\text{m}}$ and $L'_{\text{CO}(1-0)}^{\text{mid-}J \text{ CO}}$ (assuming $r_{31} = 1$) suggests that the excitation of the low- J CO rotational levels is likely to be near thermal.

Next, we follow the description in Magdis et al. (2012) to derive the metallicity-dependent dust-to-gas mass ratio δ_{GDR} . We note that the absorption metallicities of the two DLAs are known (Møller & Christensen 2020; Kanekar et al. 2020), but these correspond to the pencil beam along the QSO sightline. Due to metallicity gradients (e.g. Christensen et al. 2014), the metallicity of the host galaxy in which the molecular gas is located may be different from that measured in absorption. For consistency with the approach in Magdis et al. (2012), we estimate the metallicities from the Fundamental Mass Metallicity relation (Mannucci et al. 2010) rescaled to the Pettini & Pagel (2004) metallicity scale. We propagate the uncertainties on the best-fit M_\star

Table 4. Molecular gas masses from different methods.

DLA galaxy	$L'_{\text{CO}(1-0)}^{\text{mid-}J \text{ CO}} \times 10^{10}$ ($r_{31} = 0.55$) [K km s ⁻¹ pc ²]	$L'_{\text{CO}(1-0)}^{\text{mid-}J \text{ CO}} \times 10^{10}$ ($r_{31} = 1$) [K km s ⁻¹ pc ²]	$L'_{\text{CO}(1-0)}^{850\mu\text{m}} \times 10^{10}$ [K km s ⁻¹ pc ²]	$M_{\text{mol}}^{850\mu\text{m}} \times 10^{10}$ [M _⊙]	$M_{\text{mol}}^{\text{CO}} \times 10^{10}$ ($r_{31} = 0.55$) [M _⊙]	$M_{\text{mol}}^{\text{CO}} \times 10^{10}$ ($r_{31} = 1$) [M _⊙]	$M_{\text{mol}}^{\text{dust}} \times 10^{10}$ [M _⊙]
B1228-113	3.40 ± 0.15	1.869 ± 0.080	1.91 ^{+0.78} _{-0.67}	8.3 ^{+3.4} _{-2.9}	14.82 ± 0.65	8.15 ± 0.35	4.6 ^{+8.5} _{-3.5}
J0918+1636	4.56 ± 0.29	2.51 ± 0.16	2.29 ^{+0.99} _{-0.83}	9.98 ^{+4.3} _{-3.6}	19.9 ± 1.3	10.94 ± 0.70	2.8 ^{+5.6} _{-1.8}

Notes: $L'_{\text{CO}(1-0)}^{850\mu\text{m}}$ is the CO(1–0) luminosity derived from the rest frame 850μm luminosity using the $L'_{\text{CO}(1-0)}^{850\mu\text{m}} - L_{850\mu\text{m}}$ scaling relation of [Scoville et al. \(2016\)](#), $L'_{\text{CO}(1-0)}^{\text{mid-}J \text{ CO}}$ is the CO(1–0) luminosity derived from the mid- J transitions ([Kanekar et al. 2020](#)). We provide estimates of $L'_{\text{CO}(1-0)}^{\text{mid-}J \text{ CO}}$ and the molecular gas mass $M_{\text{mol}}^{\text{CO}}$ based on two different values of the CO line luminosity ratio r_{31} , assuming $r_{31} = 0.55, 1.0$. $M_{\text{mol}}^{\text{dust}}$ is derived from an assumed dust-to-gas ratio following [Magdis et al. \(2012\)](#). See text for a discussion of these values. All quantities have been scaled to the cosmology assumed in this paper.

and SFR values, and the ~ 0.2 dex uncertainty on the metallicity calibration to δ_{GDR} . We derive $12+\log(\text{O}/\text{H}) = 8.40 \pm 0.2$ and 8.49 ± 0.2 ($[\text{M}/\text{H}] = -0.29$ and -0.20 , respectively) for DLA B1228–113 and DLA J0918+1636, respectively.² While the dispersion around the fundamental relation is very small (0.05 dex) at low redshifts, the dispersion increases to 0.2–0.3 dex at $z \gtrsim 2$ ([Mannucci et al. 2010](#)). Taking this dispersion into account, the estimated host galaxy metallicities are consistent with a solar value. This supports the choice of an $\alpha(\text{CO})$ conversion factor of $4.36 \text{ M}_{\odot} (\text{K km s}^{-1} \text{ pc}^2)^{-1}$. However, if the galaxies have a subsolar metallicity, $\alpha(\text{CO})$ could be greater than the assumed value.

Based on the above, we estimate $\delta_{\text{GDR}} = 167^{+298}_{-94}$ for DLA B1228–113 and 136^{+243}_{-77} for DLA J0918+1636, where the errors include a 0.2 dex uncertainty on the metallicity and a 0.15 dex scatter on the metallicity- δ_{GDR} relation.

The dust mass is related to the total gas mass by the following relation ([Magdis et al. 2012](#)):

$$\delta_{\text{GDR}} M_{\text{dust}} = M_{\text{gas}} \equiv M_{\text{H I}} + M_{\text{mol}} \quad (1)$$

Recent H I 21-cm line stacking experiments in star-forming galaxies at $z \approx 1$ have found that, on average, $M_{\text{H I}} \approx M_{\text{mol}}$ ([Chowdhury et al. 2020, 2021](#)). This yields

$$\delta_{\text{GDR}} M_{\text{dust}} \approx 2 \times M_{\text{mol}} \quad (2)$$

Using the dust masses from our MBB fits, we obtain molecular gas masses reported in Table 4. The main uncertainties of this method include the assumption that the galaxies follow the Fundamental Mass Metallicity relation mentioned, the fraction of molecular gas in the total gas mass, and the dust mass absorption coefficient. Moreover, δ_{GDR} is calibrated to local main-sequence galaxies. [Magdis et al. \(2012\)](#) argue that assuming no redshift evolution in the dust-to-gas mass ratio is unlikely to be a major concern for their method. They also find that high redshift main-sequence galaxies and SMGs follow approximately the same relation although SMGs tend to have a slightly higher δ_{GDR} at a given metallicity.

For both galaxies we find that $M_{\text{mol}}^{\text{dust}}$ is significantly lower than $M_{\text{mol}}^{\text{CO}}$ if we assume $r_{31} = 0.55$ ([Kanekar et al. 2020](#)). However, applying the updated $r_{31} = 1$ line luminosity ratio we find that the molecular gas masses derived from the two methods agree within the errors for DLA B1228–113. In the case of DLA J0918+1636, $M_{\text{mol}}^{\text{dust}}$

is lower than $M_{\text{mol}}^{\text{CO}}$ even for $r_{31} \approx 1$, although formally consistent within the errors. For this galaxy, the thermalised CO excitation conditions up to the $J = 4$ level suggest that α_{CO} may be lower than $4.36 \text{ M}_{\odot} (\text{K km s}^{-1} \text{ pc}^2)^{-1}$, since α_{CO} is proportional to \sqrt{n}/T . If so, this would imply a lower $M_{\text{mol}}^{\text{CO}}$, in even better agreement with the $M_{\text{mol}}^{\text{dust}}$ value.

The assumptions discussed above, their validity, and the consequences for the final estimates have been the focus of dedicated in-depth investigations over the years ([Magdis et al. 2012](#); [Scoville et al. 2016](#), and many others). Given the current data availability, more sophisticated calculations are beyond the scope of this work.

4 CONCLUSIONS

We study the CO spectral line energy distributions (CO SLEDs) of absorption-selected galaxies previously detected in a low J rotational CO transition ([Fynbo et al. 2018](#); [Neeleman et al. 2018](#); [Kanekar et al. 2018](#); [Kanekar et al. 2020](#)). The absorbers were originally selected to have high metallicity, and therefore are likely to trace high stellar mass host galaxies ([Christensen et al. 2014](#)). We detect all but one targeted higher J rotational transitions in the observed galaxies. Using an automated emission line finder we do not detect any additional galaxies associated with the absorbers in our observations. The CO line ratios in two out of four absorption-selected galaxies are low and consistent with the CO line ratios observed in the Milky Way inner disk.

Two absorption-selected galaxies show elevated CO line ratios with respect to the other absorption-selected galaxies in this sample. The lowest redshift galaxy in our sample (DLA J2335+1501 at $z_{\text{abs}} = 0.6798$) shows a CO SLED similar to galaxies on and above the star-forming main sequence at higher redshift, but also consistent with that of the Milky Way. DLA B0551–366 ($z_{\text{abs}} = 1.9622$) too has a CO SLED consistent with that of the Milky Way inner disk, and below the CO SLED of main sequence galaxies at $z \sim 1.5$.

The other two galaxies, DLA B1228–113 at $z = 2.1929$ and DLA J0918+1636 at $z = 2.5832$, show CO line ratios above that of the Milky Way inner disk. The former shows excitation conditions below the average of main-sequence galaxies at similar redshifts, while the latter shows thermalised excitation in the CO(4–3) transition which we identify as the peak of the CO SLED.

Our results show that the excitation conditions in the ISM of absorption-selected galaxies can range from low excitation similar to the inner disk of the Milky Way up to thermal excitation of the mid- J levels. Combined with the results from [Klitsch et al. \(2019\)](#), who presented the first study of CO SLEDs in absorption-selected galaxies at

² For reference, for DLA B1228–113 this estimate is consistent with $[\text{M}/\text{H}] = -0.03^{+0.18}_{-0.13}$ estimated from the absorption-based mass-metallicity relation ([Møller et al. 2013](#)). The latter is not applicable for DLA J0918+1636, where the more likely DLA galaxy is at a closer projected separation to the quasar ([Fynbo et al. 2013](#)).

$z \sim 0.5$, we now have a sample of seven absorption-selected galaxies with information on their CO SLED. Four of these are at intermediate redshifts $z \sim 0.5 - 0.7$ and three at high redshift, $z \gtrsim 2$. At intermediate redshifts, the range of ISM excitation conditions reflect a range of galaxy types [one potential starburst, two galaxies hosting an active galactic nucleus out of which one is potentially a starburst galaxy (Klitsch et al. 2019) and one main-sequence galaxy]. At $z \sim 2$, two of the galaxies presented here have measured stellar masses and SFRs, and lie within the spread of the star-forming main-sequence at their redshifts (Whitaker et al. 2014). Absorption-selected galaxies at $z \sim 2$ show a range of excitation conditions comparable to that found in main-sequence galaxies at similar redshifts (Brisbin et al. 2019; Boogaard et al. 2020; Valentino et al. 2020; Henríquez-Brocal et al. 2021).

Absorption-selected galaxies are detected by a combination of the neutral gas cross-section as well as the luminosity of the absorber host galaxy which again is correlated with the galaxy- and absorber metallicity. Several studies have compared the properties of absorption- and emission-selected samples. Krogager et al. (2017) find that an absorption-selected galaxy sample covers a larger span of the underlying galaxy luminosity function compared to flux-limited samples. Rhodin et al. (2018) find that absorption-selected galaxies at $z \sim 0.7$ follow the main-sequence at that redshift. However, at the high-mass end [$\log(M_\star/M_\odot) > 10.5$], absorption-selected galaxies tend to fall below the star-forming main-sequence. At $z \sim 2$ Rhodin et al. (2021) report that the absorption-selected galaxies identified to date belong to the category of main-sequence galaxies at that redshift, albeit extrapolated to a lower-mass range ($10^8 - 10^{10} M_\odot$) compared to emission-selected samples. Finally, based on the molecular gas mass derivations and modest SFRs, Kanekar et al. (2018) report a low star formation efficiency in absorption-selected galaxies at $z \sim 0.7$ compared to emission-selected main-sequence galaxies at $z = 0$ and $z = 2$.

Overall, absorption-selected galaxies have been found to belong to a range of different galaxy types with stellar masses towards the lower mass end compared to emission-selections. We conclude that the range of excitation conditions mirror the spread in galaxy types. Whether a specific galaxy type is overrepresented as suggested by Klitsch et al. (2019) can only be addressed with a statistically significant sample. A remaining question is also how the variety of excitation conditions and CO SLEDs in absorption-selected galaxies are connected to other physical properties of the galaxies, and whether there are systematic variations of the CO SLEDs with redshifts.

For DLA B1228–113 and DLA J0918+1636, we investigated whether the $L'_{\text{CO}(1-0)}$ and the molecular gas mass derived from different scaling relations to the dust luminosity (this work) and mid- J CO transitions (Kanekar et al. 2020) are consistent with each other. For both galaxies, we find that $L'_{\text{CO}(1-0)}$ derived from the dust luminosity is lower than $L'_{\text{CO}(1-0)}$ derived from the mid- J CO transitions by a factor of ~ 2 when assuming a sub-thermal line luminosity ratio of $r_{31} = 0.55$. However, applying a line luminosity ratio of $r_{31} = 1$, we find that $L'_{\text{CO}(1-0)}$ derived from the two different methods are in reasonable agreement. The molecular gas masses derived from the dust scaling and CO emission also agree within the uncertainties of the respective conversions when assuming $r_{31} = 1$ for DLA B1228–113 and for DLA J0918+1636. It thus appears likely that the molecular gas masses of these two absorption-selected galaxies are a factor of ≈ 2 lower than earlier estimates in the literature, based on sub-thermal excitation of the mid- J rotational levels.

It is important to emphasize that our study is limited by the coverage of only a few observed CO transitions for each galaxy, and

especially does not include the J(1–0) transition. As the CO line excitation is a non-linear, non-monotonic function, there may be ambiguities in interpreting the measured line excitation ratios when these are anchored at transitions above the CO(1–0) transition, as we have done here.

ACKNOWLEDGEMENTS

A.K. gratefully acknowledges support from the Independent Research Fund Denmark via grant number DFF 8021-00130. F.V. acknowledges support from the Carlsberg Foundation Research Grant CF18-0388 “Galaxies: Rise and Death”. N.K. acknowledges support from the Department of Atomic Energy, under project 12-R&D-TFR-5.02-0700. J.P.U.F. acknowledges support from the Carlsberg Foundation. The Cosmic Dawn Center (DAWN) is funded by the Danish National Research Foundation under grant No.140. M.N. acknowledges support from ERC Advanced grant 740246 (Cosmic_Gas). This paper makes use of the following ALMA data: ADS/JAO.ALMA#2019.1.01457.S. ALMA is a partnership of ESO (representing its member states), NSF (USA) and NINS (Japan), together with NRC (Canada), MOST and ASIAA (Taiwan), and KASI (Republic of Korea), in cooperation with the Republic of Chile. The Joint ALMA Observatory is operated by ESO, AUI/NRAO and NAOJ. This research made use of Astropy³ a community-developed core Python package for Astronomy (Astropy Collaboration et al. 2013; Price-Whelan et al. 2018). This research has made use of NASA’s Astrophysics Data System.

DATA AVAILABILITY

The data underlying this article are available in the respective observatories online archives. Used ALMA data is available through the ALMA Science Archive (<https://almascience.eso.org/asax/>). Project IDs are given in Section 2. Based on observations collected at the European Southern Observatory under ESO programme 197.A-0384.

REFERENCES

- Andersen A. C., 2007, in Kerschbaum F., Charbonnel C., Wing R. F., eds, *Astronomical Society of the Pacific Conference Series Vol. 378, Why Galaxies Care About AGB Stars: Their Importance as Actors and Probes*. p. 170 (arXiv:astro-ph/0702618)
- Aravena M., et al., 2019, *ApJ*, **882**, 136
- Aravena M., et al., 2020, arXiv:2006.04284 [astro-ph]
- Astropy Collaboration et al., 2013, *A&A*, **558**, A33
- Bayet E., Gerin M., Phillips T. G., Contursi A., 2004, *A&A*, **427**, 45
- Berta S., Lutz D., Genzel R., Förster-Schreiber N. M., Tacconi L. J., 2016, *A&A*, **587**, A73
- Bolatto A. D., Wolfire M., Leroy A. K., 2013, *ARA&A*, **51**, 207
- Boogaard L. A., et al., 2020, *ApJ*, **902**, 109
- Bothwell M. S., et al., 2013, *MNRAS*, **429**, 3047
- Briggs D. S., 1995, in *American Astronomical Society Meeting Abstracts*. p. 112.02
- Brisbin D., Aravena M., Daddi E., Dannerbauer H., Decarli R., González-López J., Riechers D., Wagg J., 2019, *A&A*, **628**, A104
- Burbidge E. M., Beaver E. A., Cohen R. D., Junkkarinen V. T., Lyons R. W., 1996, *The Astronomical Journal*, **112**, 2533
- Chabrier G., 2003, *PASP*, **115**, 763

³ <http://www.astropy.org>

Chen H.-W., Kennicutt R. C., Rauch M., 2005, *ApJ*, 620, 703

Chowdhury A., Kanekar N., Chengalur J. N., Sethi S., Dwarakanath K. S., 2020, *Nature*, 586, 369

Chowdhury A., Kanekar N., Das B., Dwarakanath K. S., Sethi S., 2021, *ApJ*, 913, L24

Christensen L., Møller P., Fynbo J. P. U., Zafar T., 2014, *MNRAS*, 445, 225

Daddi E., et al., 2015, *A&A*, 577, A46

Dessauges-Zavadsky M., et al., 2015, *A&A*, 577, A50

Fixsen D. J., Bennett C. L., Mather J. C., 1999, *ApJ*, 526, 207

Fynbo J. P. U., et al., 2013, *MNRAS*, 436, 361

Fynbo J. P. U., et al., 2018, *MNRAS*, 479, 2126

Greve T. R., et al., 2014, *ApJ*, 794, 142

Harrington K. C., et al., 2021, *ApJ*, 908, 95

Henríquez-Brocal K., et al., 2021, arXiv e-prints, p. arXiv:2109.01684

Ivison R. J., Papadopoulos P. P., Smail I., Greve T. R., Thomson A. P., Xilouris E. M., Chapman S. C., 2011, *MNRAS*, 412, 1913

Kaasinen M., et al., 2019, *ApJ*, 880, 15

Kamenetzky J., Rangwala N., Glenn J., Maloney P. R., Conley A., 2014, *ApJ*, 795, 174

Kamenetzky J., Rangwala N., Glenn J., 2017, *MNRAS*, 471, 2917

Kanekar N., et al., 2018, *ApJL*, 856, L23

Kanekar N., Prochaska J. X., Neeleman M., Christensen L., Møller P., Zwaan M. A., Fynbo J. P. U., Dessauges-Zavadsky M., 2020, *ApJ*, 901, L5

Klitsch A., Péroux C., Zwaan M. A., Smail I., Oteo I., Biggs A. D., Popping G., Swinbank A. M., 2018, *MNRAS*, 475, 492

Klitsch A., et al., 2019, *MNRAS*, 482, L65

Krogager J.-K., Møller P., Fynbo J. P. U., Noterdaeme P., 2017, *MNRAS*, 469, 2959

Lu N., et al., 2017, *ApJS*, 230, 1

Magdis G. E., et al., 2012, *ApJ*, 760, 6

Mannucci F., Cresci G., Maiolino R., Marconi A., Gnerucci A., 2010, *MNRAS*, 408, 2115

McMullin J. P., Waters B., Schiebel D., Young W., Golap K., 2007, *Astronomical Data Analysis Software and Systems XVI*, 376, 127

Møller P., Christensen L., 2020, *MNRAS*, 492, 4805

Møller P., Fynbo J. P. U., Ledoux C., Nilsson K. K., 2013, *MNRAS*, 430, 2680

Møller P., et al., 2018, *MNRAS*, 474, 4039

Neeleman M., Kanekar N., Prochaska J. X., Christensen L., Dessauges-Zavadsky M., Fynbo J. P. U., Møller P., Zwaan M. A., 2018, *ApJ*, 856, L12

Neeleman M., Prochaska J. X., Kanekar N., Rafelski M., 2020, *Nature*, 581, 269

Péroux C., et al., 2019, *MNRAS*, 485, 1595

Pettini M., Pagel B. E. J., 2004, *MNRAS*, 348, L59

Price-Whelan A. M., et al., 2018, *AJ*, 156, 123

Rhodin N. H. P., Christensen L., Møller P., Zafar T., Fynbo J. P. U., 2018, *A&A*, 618, A129

Rhodin N. H. P., Krogager J. K., Christensen L., Valentino F., Heintz K. E., Møller P., Zafar T., Fynbo J. P. U., 2021, *MNRAS*, 506, 546

Rosenberg M. J. F., et al., 2015, *ApJ*, 801, 72

Schlaflly E. F., Finkbeiner D. P., 2011, *ApJ*, 737, 103

Schreiber C., Elbaz D., Pannella M., Ciesla L., Wang T., Franco M., 2018, *A&A*, 609, A30

Scoville N., et al., 2016, *ApJ*, 820, 83

Serra P., et al., 2015, *MNRAS*, 448, 1922

Szakacs R., et al., 2021, *MNRAS*, 505, 4746

Tacconi L. J., Genzel R., Sternberg A., 2020, *ARA&A*, 58, 157

Valentino F., et al., 2020, *A&A*, 641, A155

Weiß A., Walter F., Scoville N. Z., 2005, *A&A*, 438, 533

Whitaker K. E., et al., 2014, *ApJ*, 795, 104

Wolfe A. M., Gawiser E., Prochaska J. X., 2005, *ARA&A*, 43, 861

da Cunha E., Charlot S., Elbaz D., 2008, *MNRAS*, 388, 1595

da Cunha E., et al., 2015, *ApJ*, 806, 110

van der Werf P. P., et al., 2010, *A*, 518, L42

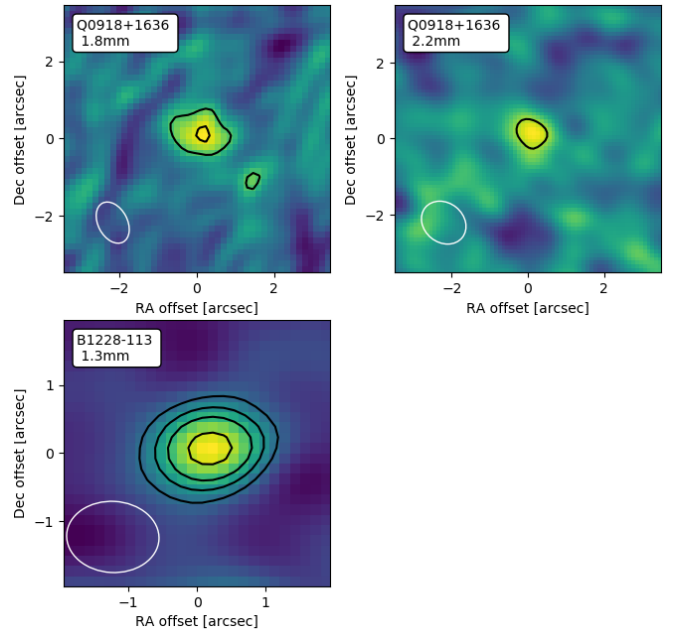


Figure A1. ALMA continuum images of DLA B1228-113 and DLA J0918+1636. The central wavelength of the continuum image is indicated at the top left of each panel. The first contour in each panel is at 1σ , with successive contours increasing by 1σ .

APPENDIX A: CONTINUUM IMAGES AND SED FITS.

This appendix provides information on the SED fits to the optical, near-IR and sub-mm continuum data obtained with MAGPHYS (da Cunha et al. 2008).

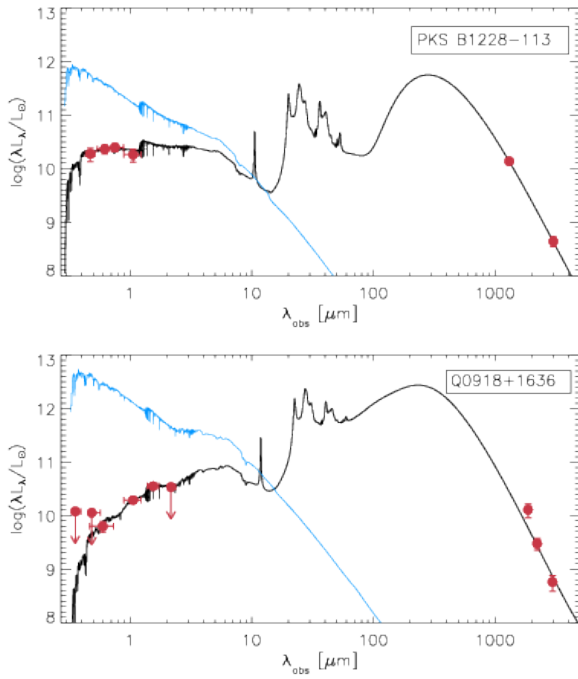
In Fig. A1 we show the sub-mm continuum images of DLA B1228-113 and DLA J0918+1636. The optical and near-IR data for DLA J0918+1636 were presented originally in Fynbo et al. (2018); these values are included in Table A1, for completeness. For DLA B1228-113, optical magnitudes are derived from MUSE data extracted from the spectral data cube within an aperture of 2 arcsec. The coadded 1-dimensional spectrum is multiplied with the SDSS filter transmission curves to derive AB magnitudes. The near-IR photometry is presented in Neeleman et al. (2018). The optical and near-IR photometric data were corrected for Galactic reddening Schlafly & Finkbeiner (2011) and, along with the ALMA continuum flux densities, were used as inputs to MAGPHYS. Fig. A2 present the best fit SED models for the two galaxies, while Table A2 the resulting best fit values of the stellar mass, the dust mass, and the SFR, along with the 68% confidence intervals.

This paper has been typeset from a \LaTeX file prepared by the author.

Table A1. Photometry of DLA B1228–113 and DLA J0918+1636

Band	J0918+1636	B1228–113
<i>u</i>	>26.5 (3σ)	—
<i>g</i>	>26.2 (3σ)	25.3±0.3
<i>r</i>	—	24.7±0.2
<i>i</i>	—	24.4±0.2
<i>F</i> 606W	26.59±0.25	—
<i>F</i> 105W	24.70±0.13	24.36±0.3
<i>F</i> 160W	23.63±0.07	—
<i>K_S</i>	>23.3 (3σ)	—
ALMA 1.33 mm	—	627 ± 50
ALMA 1.86 mm	565±162	—
ALMA 2.21 mm	156±39	—
ALMA 2.95 mm	40±13	46±10

Notes: For the optical and near-IR data of J0918+1636, a 2 arcsec aperture diameter was used. All optical and near-IR magnitudes are in AB units (Fynbo et al. 2018). The table values have not been corrected for Galactic reddening. Continuum flux densities in the ALMA bands are in units of μJy .

**Figure A2.** SED fits obtained with MAGPHYS for DLA B1228–113 and DLA J0918+1636.**Table A2.** Best-fit values of parameters from MAGPHYS obtained when fixing the redshift to that of the two galaxies. Uncertainties represent 68% confidence intervals.

	J0918+1636	B1228–113
SFR [M_{\odot}/yr]	229 ⁺¹⁵¹ _{−91}	87 ⁺³⁹ _{−28}
$\log(M_{*}/M_{\odot})$	10.49 ^{+0.16} _{−0.11}	10.13 ^{+0.34} _{−0.23}
$\log(M_{\text{dust}}/M_{\odot})$	8.62 ^{+0.16} _{−0.15}	8.74 ^{+0.10} _{−0.12}